

Appendix

A.1 Cation Ordering

As already discussed in Section 2.2.4.1 the typical cation ordering of the chalcopyrite structure is reflected in the XRD-spectra by the appearance of additional reflections (group (iii) in Section 2.2.4.1) referred to as super lattice reflections. In the case of vanishing anion displacement $u = 0$ the structure factor of group (iii) reflections is given by

$$F_{hkl}^{(iii)} \propto f_{\text{Cu}}^2 - 2f_{\text{Cu}}f_{\text{In}} + f_{\text{In}}^2, \quad (\text{A.1})$$

i.e. the appearance of these reflections originates from the difference in the atomic scattering factors of group I and group III cation lattice sites in the chalcopyrite structure. In the case of $u \neq 0.25$ there is a small additional contribution to the scattering factor which depends on u as well as the specific (h, k, l) indices. In a sphalerite lattice where the cations sublattice sites are randomly occupied by group I and group III atoms the difference cancels out on a macroscopic scale and group (iii) reflections can not be observed. In this sense the intensity of these reflections is a direct measure for the degree of chalcopyrite ordering in the crystal lattice. However, the interpretation is not straightforward since the magnitude of the structure factors of the group (iii) reflections is also very sensitive to the occupation of the cation sublattices and to the displacement of the anion in the chalcopyrite lattice. Therefore a precise analysis of the intensities of group (iii) reflections can also provide informations about lattice imperfections such as vacancies or antisite defects. Albin [166] showed a correlation between the intensity of group (iii) reflexes and the molecularity $m = [\text{Cu}]/([\text{Cu}] + [\text{Ga}])$ of CuGaSe_2 thin films, which was in agreement with calculated structure factor values F_{hkl} for a lattice containing copper vacancies and gallium atoms at copper sites.

The relative intensity of group (iii) reflections with respect to the (112) reflection was already discussed in Section 3.3 in order to demonstrate the improvement in lattice ordering during the recrystallization step of the film growth process. In order to evaluate the influence of structural deviations from an ideal chalcopyrite unit cell onto the group (iii) reflections the effects of

- cation order/disorder transitions,
- deviations from molecularity,
- changes in the anion displacement u , and

- the isovalent substitution of In with Ga.

have been incorporated in the structure factor calculations (Section 2.2.4). Since each of these effects influences the intensity of individual group (iii) reflections in a different way the role of each factor can, at least qualitatively, be determined when comparing the calculations to trends of the experimental data. Several calculated examples and a comparison to experimental data will be given in the following.

Structure factors were calculated according to Equation (2.6). The atomic form factors f_α have been altered to account for the deviations from the ideal occupation of lattice sites. In the perfect chalcopyrite crystal group I atom sites are occupied by Cu, group III atom sites are occupied by In, and group VI atom sites are occupied by S. An undisturbed sulfur sublattice has been assumed in all calculations, i.e. $f_{VI} = f_S$. It has to be noted that texture effects have not been taken into account here. This seems to be justified by the fact that no substantial discrepancies between the calculated zincblende (group (i)) XRD reflections and the experimental data could be found in this work.

Cation order/disorder transitions As mentioned above cation antisite disorder, such as In at Cu lattice sites (In_{Cu}) and vice versa (Cu_{In}), ultimately leads to the cubic sphalerite structure. Pamplin et. al. [22] have proposed a disorder parameter

$$\delta_{\text{disorder}} = \frac{\text{Cu}_{\text{In}}}{\text{Cu}_{\text{Cu}}} = \frac{\text{In}_{\text{Cu}}}{\text{In}_{\text{In}}}, \quad (\text{A.2})$$

which ranges from zero in the case of perfect ordering to unity for perfect disorder. Under the presence of antisite disorder the atomic scattering factors at the group I atom lattice site and the group III atom lattice site change as follows

$$\begin{aligned} f_{\text{I}} &= \left(\delta_{\text{disorder}} + 1 \right)^{-1} f_{\text{Cu}} + \left(\frac{1}{\delta_{\text{disorder}}} + 1 \right)^{-1} f_{\text{In}}, \\ f_{\text{III}} &= \left(\delta_{\text{disorder}} + 1 \right)^{-1} f_{\text{In}} + \left(\frac{1}{\delta_{\text{disorder}}} + 1 \right)^{-1} f_{\text{Cu}}. \end{aligned} \quad (\text{A.3})$$

Anion displacement The influence of variations in the anion displacement can be calculated in a straight forward manner by accounting for the change of the fractional coordinates of the atomic position of the S-atom in Equation (2.6).

In-Ga substitution The incorporation of Ga at group III lattice sites is modeled by assuming a statistical substitution of In by Ga. For the atomic scattering factor f_{III} it follows

$$f_{\text{III}} = (1 - x) f_{\text{In}} + x f_{\text{Ga}}, \quad (\text{A.4})$$

where x refers to the $[\text{Ga}]/([\text{In}] + [\text{Ga}])$ ratio. Lattice constant a and c and the anion displacement u are assumed to vary linearly with x according to Vegard's Law (see Figure 2.13).

Deviations in molecularity Defect-dependent structure factors for a Cu-deficient lattice have been calculated for the CuInS₂ lattice following a similar approach as in [166]. The considerations have been restricted to the one phase region of CuInS₂ along the pseudo-binary line (Cu₂S)_m-(In₂S₃)_{1-m}, where m refers to the molecularity $[\text{Cu}]/([\text{Cu}] + [\text{In}])$. Furthermore, it will be assumed that the anions form a perfect lattice and that the structure of the defected compound will be that of a defect adamantine with decreasing Cu-content (Cu excess can not be accommodated by the chalcopyrite lattice and will rather lead to Cu_{2-x}S segregation). For the normalized atomic fractions of the defect compound follows:

$$(\text{Cu}_2\text{S})_m(\text{In}_2\text{S}_3)_{1-m} \rightarrow \text{Cu}_{2m[2/(3-2m)]}\text{In}_{2(1-m)[2/(3-2m)]}\text{S}_2. \quad (\text{A.5})$$

From Equation (A.5) it becomes clear that with decreasing m , i.e. if the material becomes Cu-poor, one In atom is added to the lattice for every 3 Cu atoms removed from it:

$$\frac{\Delta[\text{In}]}{\Delta[\text{Cu}]} = \frac{2(1-m)[2/(3-2m)] - 1}{1 - 2m[2/(3-2m)]} = \frac{1}{3}. \quad (\text{A.6})$$

This suggests that defects pairs of the type $2V_{\text{Cu}} + \text{In}_{\text{Cu}}$ are introduced into the lattice with decreasing molecularity, as such a defect pair was found to be the energetically most favorable type of defect in Cu-chalcopyrites by Zunger et al. [124]. In the considered case it is further assumed that only Ga atoms substitute for Cu at group I atomic sites. Such a situation refers to an incorporation of Ga at group I and group III lattice sites in contrast to the isovalent substitution at group III lattice sites only as considered above. In such a case the atomic form factors read as follows:

$$\begin{aligned} f_{\text{I}} &= 2m[2/(3-2m)]f_{\text{Cu}} + (2(1-m)[2/(3-2m)] - 1)f_{\text{Ga}}, \\ f_{\text{III}} &= (1-x)f_{\text{In}} + xf_{\text{Ga}}. \end{aligned} \quad (\text{A.7})$$

Calculations The intensity of some of the most intense group (iii) reflections i.e. (101), (121), (301) with respect to the (112) reflection have been calculated for each of the cases discussed above. CuInS₂ lattice constants and the anion displacement have been taken from [24] (see Table 1.1). Intensity values have been obtained by applying the corrections as discussed in Appendix A.3.

Figure A.1 shows the obtained intensity ratios for a CuInS₂ thin film of 2.5 μm thickness. As discussed above cation antisite disorder or in other words the transition from a chalcopyrite to a sphalerite lattice leads to a significant reduction of the group (iii) intensities. As can be seen in the Figure A.1 (a) a disorder parameter of 0.2 causes a decrease in XRD intensity down to a half or even one third of the initial intensity of the undisturbed lattice. Large changes are also indicated by Figure A.1 (c) where the anion displacement parameters u is varied. The isovalent substitution of In by Ga does not greatly effect the group (iii) intensities (Figure A.1 (b)). And even the incorporation of Ga at group I atom lattice sites does only affect the (101) reflection significantly. Thus the figure demonstrates that whereas structural changes lead to quite large changes in the group (iii) the incorporation

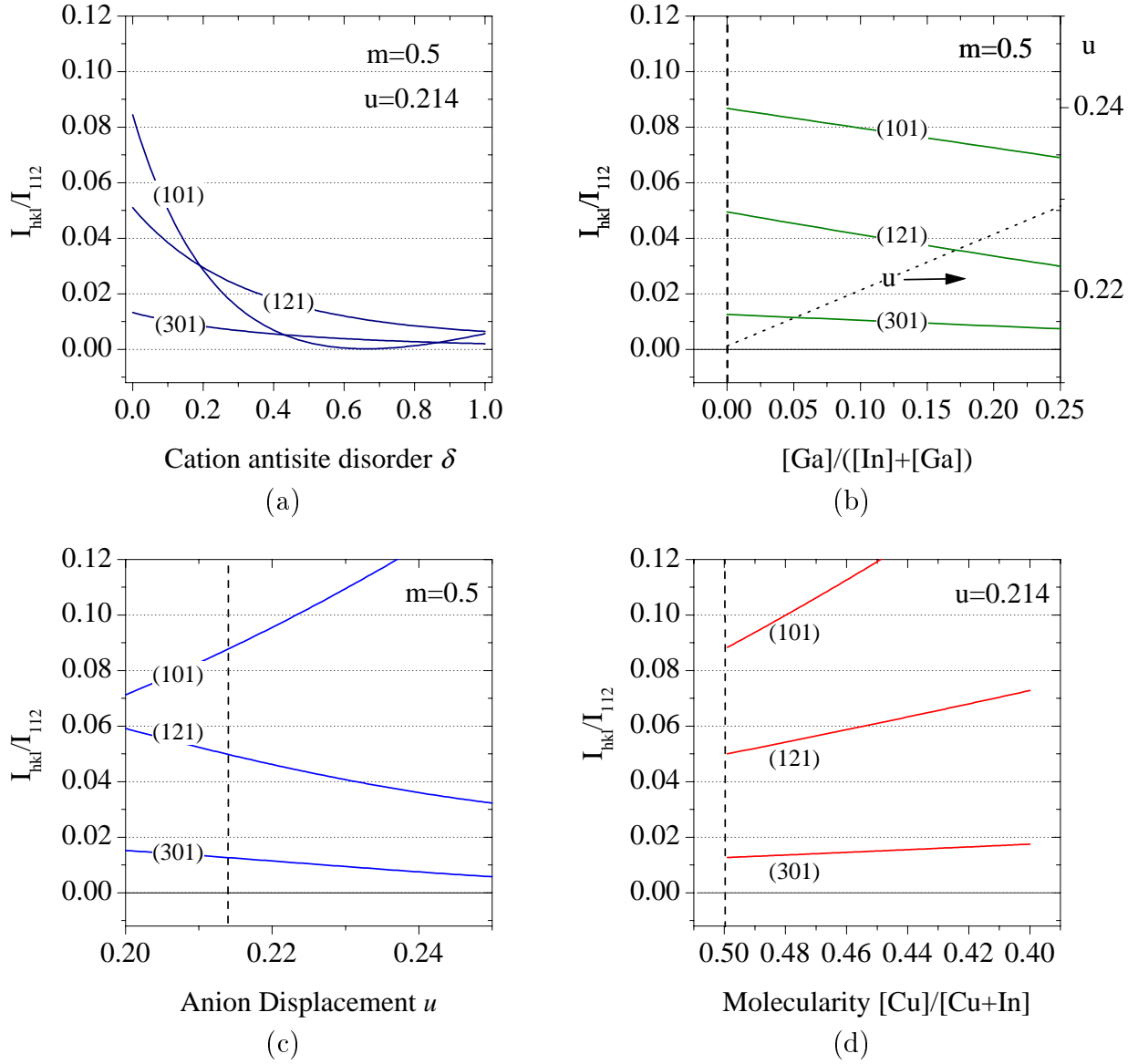


Figure A.1: Calculated intensities of some group (iii) reflections (chalcopyrite superlattice) relative to the (112) intensity for a CuInS₂ thin film of 2.5 μm thickness of (a) Cu-In antisite disorder on the cation sublattice (fixed u -value), (b) varied Ga-In substitution on the atom III sublattice (u varied acc. to Figure 2.13), (c) varied anion displacement, (d) varied molecularity, i.e. Ga_{Cu} + 2V_{Cu}.

of Ga does not have such a big effect. The ratio between the (101) intensity and the (121) intensity can serve as an indicator whether deviations in group (iii) intensity are due to disorder effects or changes in anion displacement.

Cu(In_{1-x}Ga_x)S₂-thin films - experimental data Ga-incorporation in the CuInS₂ surface phase of sequentially prepared layers has a great influence on the chalcopyrite superlattice peaks. Figure A.2 compares the three most intense group (iii) reflections normalized to the (112) intensity of a Ga-free reference sample and two samples with a nominal [Ga]/([In] + [Ga]) ratio of 0.05 and 0.14 (according to SNMS), respectively (Table 3.6). The integrated peak intensities as a function of Ga-content are plotted in Figure A.3. The dashed lines in the plot correspond to the calculated intensity of a layer of 2 μm thickness. There is a clear increase in the integrated peak-intensity of all group (iii) intensities as a result of Ga-incorporation from values clearly below the calculated intensities to values which agree very well with the calculations. With respect to the calculations presented in the previous section this clearly indicates an increase in the structural quality of Ga-containing samples. i.e. the significant increase in the (101) intensity has to be assigned to an improvement in cation ordering. Best agreement between experimental and calculated values could be reached when assuming a fixed [Ga]/([In] + [Ga]) ratio of the group III sublattice and varying the anion displacement. Table A.1 lists measured and calculated

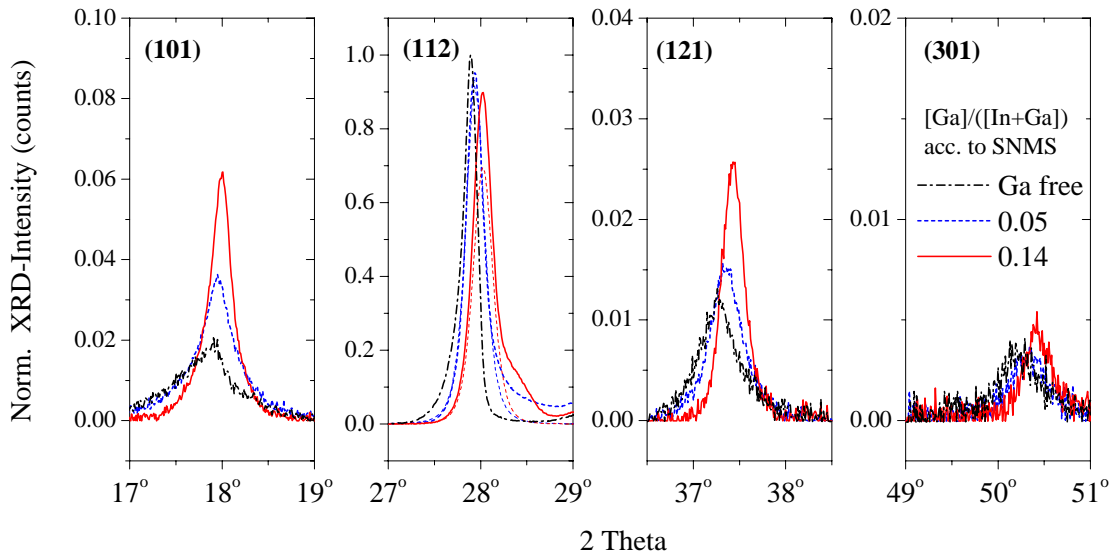
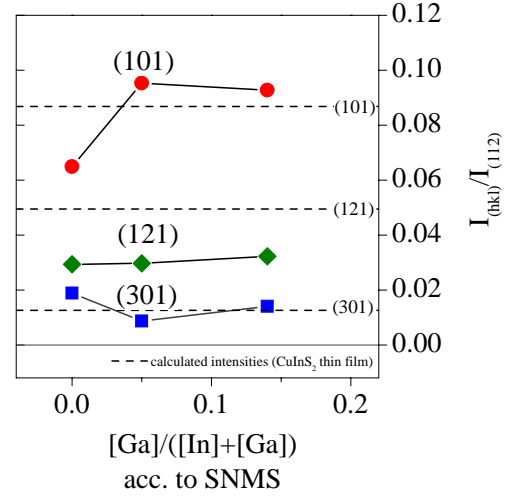


Figure A.2: XRD super lattice reflections of CuInS₂ top phase of samples with varied Ga-concentration in the phase.

intensities for the case of the $[\text{Ga}]/([\text{In}] + [\text{Ga}]) = 0.14$ sample in Figure A.2. The obtained values suggest a smaller displacement of the anion as published by [24], however taking into account the considerable scatter of reported u values for CuInS₂ (Table 1.1) such a deviation is not surprising. Substantial changes in molecularity induced by Ga-incorporation at

Figure A.3: Measured intensities of super lattice reflections of the CuInS_2 phase of three samples of varied $[\text{Ga}]/([\text{In}] + [\text{Ga}])$ ratio: 0.0 (squares), 0.05 (diamonds), 0.14 (circles). Dashed lines refer to calculated intensities for a CuInS_2 thin film (thickness $2\ \mu\text{m}$ using the parameters of Table 1.1.



group I atom lattice sites can be ruled out, as they should cause an increase in the intensity of the (101) reflection. Instead the slight decrease in the (101) intensity with increasing Ga-content is in qualitative agreement with the behavior predicted by the calculations, thus the incorporation of Ga into the CuInS_2 lattice acts mainly via isovalent substitution.

In conclusion, the analysis of chalcopyrite superlattice peaks can be of valuable assistance in the analysis of the degree of chalcopyrite ordering in CuInS_2 film, assuming texture related effects can be ruled out. A comparison of calculation XRD intensities and experimental data collected at Ga-free and Ga-containing thin films clearly show an improvement in cation-ordering with Ga-incorporation. The observed qualitative correlation between XRD-intensity and Ga-content agrees with the assumption that Ga in CuInS_2 is incorporated by isovalent substitution at In lattice sites.

Table A.1: Measured and calculated group (iii) intensities of Ga-containing CuInS_2 thin film.

$[\text{Ga}]/([\text{In}] + [\text{Ga}])$	hkl	I_{hkl}/I_{112} (exp.)	I_{hkl}/I_{112} (calc.)	u (calc.)	u Ref.[8]
0.14	(101)	0.928	0.928	0.235	0.222
	(121)	0.032	0.032		
	(301)	0.011	0.007		

A.2 Diffusion in Polycrystals

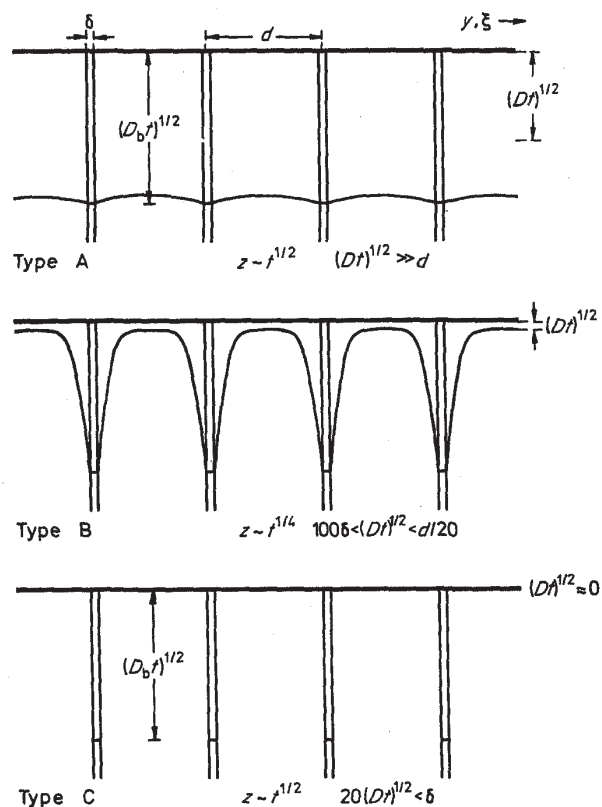


Figure A.4: Types of diffusion kinetics in a polycrystal of uniformly spaced grain boundaries, $z =$ refers to the depth of penetration of the diffusant, $t =$ anneal time, $D_b =$ grain boundary diffusion coefficient, $D =$ bulk diffusion coefficient, $d =$ grain width, $\delta =$ grain boundary width, (from [139]).

This section briefly discusses the general behavior of diffusion in polycrystals. A very detailed review of various analytical models and current experimental results describing grain boundary diffusion phenomena can be found in [139]. This discussion will be restricted to the ideal case of a semi-infinite perfect crystal with uniformly spaced grain boundaries embedded in it. Here the term grain boundary refers to a high-diffusivity, isotropic slab of uniform thickness. The surface of the crystal which is in contact with the reservoir of the diffusant is perpendicular to the grain boundaries. Diffusion within the grain may be described by the volume diffusion coefficient D and within the grain boundary slab by the grain boundary diffusion coefficient D_b , which in general is much higher than D ($D_b \gg D$).

In an experimental situation the diffusant will penetrate the crystal directly via volume diffusion from the reservoir into the grain, along grain boundaries due to grain boundary diffusion and by leakage or out-diffusion from the grain boundaries into the adjoining grains. Depending on the relative magnitudes of D and D_b and on the experimental conditions such as temperature and annealing time three types of diffusion kinetics can be distinguished. These are referred to as type A, B, and C after Harrison [167]. Figure A.4 gives an schematic illustration of the model situation just described under the three diffusion regimes.

Type A This situation refers to the case of long annealing times, small grain size, and/or a

volume diffusion coefficient not much smaller than the grain boundary diffusion coefficient. As a result the volume diffusion length \sqrt{Dt} is much larger than the spacing between the grain boundaries so contributions due to leakage from adjacent grain boundaries overlap. There are no significant differences between the concentration of the diffusant in the bulk and in the grain boundary. On a macroscopic scale the whole system appears to obey Fick's law as for a homogeneous system, i.e. there is an almost planar diffusion front parallel to the the diffusion source.

Type B Here too, grain boundary diffusion takes places with simultaneous volume diffusion from the boundary into the crystal, but in contrast to type A kinetics the grain boundary spacing is large enough for the boundaries to be considered as isolated. This results in a maximum in concentration at the grain boundary and a rapid decrease in the direction perpendicular to it. Further, the diffusant penetrates much deeper into the crystal along the grain boundary than anywhere else.

The resulting diffusion profile of the average concentration in a type B domain consists of two parts: a high-concentration steep part close to the source which is due to volume diffusion and a low-concentration flat part in the deeper region which represents grain boundary diffusion. According to Kaur [139] the condition for type B kinetics is approximately given by:

$$10\delta < (Dt)^{1/2} < d/10, \quad (\text{A.8})$$

where δ refers to the thickness of the grain boundary slab (grain boundary width).

Type C In the case of short anneal times and/or a negligibly small volume diffusion coefficient compared to the grain boundary coefficient the volume diffusion lengths will be much smaller than the grain boundary width ($(Dt)^{1/2} \ll \delta$). Then considerable diffusion only takes place within the grain boundaries.

A.2.1 Grain Boundary Diffusion in Thin Films – Gilmer-Farrell Analysis for Type B Kinetics

An analytical solution for diffusion in an array of uniformly spaced parallel grain boundaries in a specimen of finite thickness was given by Gilmer and Farrell [138]. This sections closely follows a review of Gilmer's solution given by Kaur [139].

The experimental geometry underlying the derivation is depicted in Figure A.5. The system is described by the following assumptions

- Fick's laws of diffusion are obeyed in both the crystal and the grain boundary.
- The diffusion coefficient D and D_b are isotropic and independent of concentration, position and time.
- The diffusant flow is continuous at the grain boundary/crystal interface.
- The width of the grain boundary is so small that the concentration variation across it is negligible.

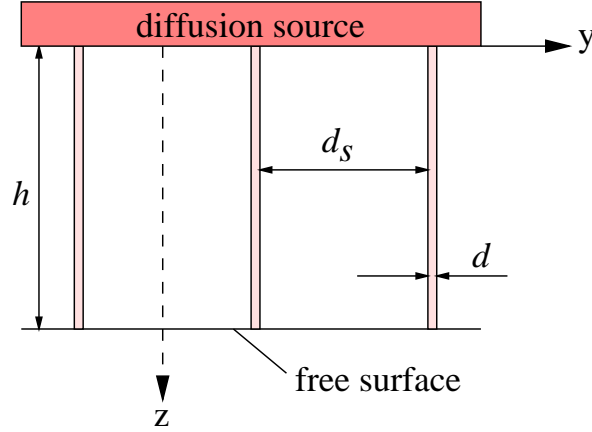


Figure A.5: Geometry of thin-film specimen used by Gilmer and Farrell [138] to derive an analytical solution for grain boundary diffusion in thin films containing uniformly spaced grain boundaries.

The diffusion equation for the system are in the grain:

$$D\nabla^2 c_g = \frac{\partial c_g}{\partial t} \quad \text{for} \quad 0 \leq y < (d_s - \delta)/2, \quad (\text{A.9})$$

and in the grain boundary

$$D_b \nabla^2 c_b = \frac{\partial c_b}{\partial t} \quad \text{for} \quad \frac{d_s - \delta}{2} < y < \frac{d_s + \delta}{2}. \quad (\text{A.10})$$

Furthermore the system is determined by the following boundary conditions. At the “walls” of the grain boundary ($y = (d_s \pm \delta)/2$) the condition is:

$$D_b \frac{\partial^2 c_g}{\partial z^2} + \frac{2D}{\delta} \frac{\partial c_g}{\partial y} = \frac{\partial c_g}{\partial t}. \quad (\text{A.11})$$

Due to the symmetry of the situation the solution must also satisfy the condition

$$\left. \frac{\partial c_g}{\partial y} \right|_{y=0} = 0. \quad (\text{A.12})$$

Gilmer and Farrell obtained an analytical solution using the technique of Fourier analysis. Without going into the details of the actual derivation the final results of their work will be described here only. According to this, the solutions can be constructed from functions of the form

$$F(y, z, t) = \sum_{n=1}^{\infty} \sum_{m=1}^{\infty} A_{nm} Y_{nm}(y) Z_n(z) T_{nm}(t) \quad (\text{A.13})$$

where Y_{nm} and Z_n are given by

$$Y_{nm} = \cos(\alpha_{nm}y), \quad (\text{A.14})$$

$$Z_n = \sin(\beta_n z), \quad (\text{A.15})$$

$$\text{and} \quad (\text{A.16})$$

$$T_{nm} = \exp(-Dt(\alpha_{nm}^2 + \beta_n^2)). \quad (\text{A.17})$$

Substituting Equation A.13 into Equation A.11 as a trial solution, the boundary condition $y = (d_s \pm \delta)/2$ reduces to

$$(\Delta - 1)\beta_n^2 - \alpha_{nm}^2 = (2\alpha_{nm}/\delta) \tan(\alpha_{nm}d_s/2), \quad (\text{A.18})$$

where Δ refers to D_b/D . The coefficients α_{nm} , β_{nm} and A_{nm} are determined by the specific boundary conditions at the free surface $z = h$.

In case of a reflecting boundary, i.e. a diffusion barrier at the surface, the additional conditions is given by

$$\left. \frac{\partial c(y, z, t)}{\partial z} \right|_{z=h} = 0. \quad (\text{A.19})$$

For coefficient β_n it follows

$$\beta_n = \frac{(2n-1)\pi}{2h}. \quad (\text{A.20})$$

Since β_n is determined by Equation A.20 values for α_{nm} can be evaluated numerically by means of the transcendental relationship given by Equation A.18. The condition of a constant source at $z = 0$ requires the solution to be of the form

$$c_g(y, z, t) = c_0 \left[1 - \sum_{n=1}^{\infty} \sum_{m=1}^{\infty} A_{nm} Y_{nm}(y) Z_n(z) T_{nm}(t) \right], \quad (\text{A.21})$$

since $F(y, 0, t) = 0$. Additionally the condition of zero initial concentration in the grain was employed by Gilmer and Farrell to determine the coefficients of the parameter A_{nm} , i.e.

$$A_{nm} = \left(\frac{16}{\alpha_{nm}d_s} \sin \frac{\alpha_{nm}d_s}{2} + \frac{8\delta}{d_s} \cos \frac{\alpha_{nm}d_s}{2} \right) \times \left[(2n-1)\pi \left(1 + \frac{\sin(\alpha_{nm}d_s)}{\alpha_{nm}d_s} + \frac{2\delta}{d_s} \cos^2 \frac{\alpha_{nm}d_s}{2} \right) \right]^{-1} \quad (\text{A.22})$$

In an experiment it is usually the average concentration \bar{c} in a thin section parallel to the film that is measured

$$\bar{c}(z, t) = \frac{2}{d} \int_0^{d_s/2} c(y, z, t) dy. \quad (\text{A.23})$$

Substituting Equation A.22 into the integral in the region $0 \leq y \leq (d_s - \delta)/2$, (the amount of diffusant in the actual grain boundary is neglected here) yields

$$\bar{c}(z, t) = c_0 \left[1 - \sum_{n=1}^{\infty} \sum_{m=1}^{\infty} \frac{2}{\alpha_{nm}d_s} A_{nm} \sin \frac{\alpha_{nm}d_s}{2} Z_n(z) T_{nm}(t) \right]. \quad (\text{A.24})$$

When numerically evaluating Equation A.24 the series has been truncated for $n > n_{trunc}$ and $m > m_{trunc}$ where

$$n_{trunc} = \frac{1}{2} \left[\left(\sqrt{-\frac{\ln(1/1000)}{Dt} \frac{2h}{\pi}} \right) + 1 \right] \quad (\text{A.25})$$

$$m_{trunc} = \frac{1}{2} \left[\left(\sqrt{-\frac{\ln(1/1000)}{Dt} \frac{d_s}{\pi}} \right) + 1 \right] \quad (\text{A.26})$$

since $T_{nm} < \frac{1}{1000}$ for $n > n_{trunc}$ or $m > m_{trunc}$.

Figure A.6 (a) shows an contour plot of a grain for $\Delta = D_b/D = 10^4$ and $d_s = h$ at different values of the reduced time $t_f = Dt/h^2$. Figure A.6 (b) shows the corresponding plots of $\log \bar{c}$.

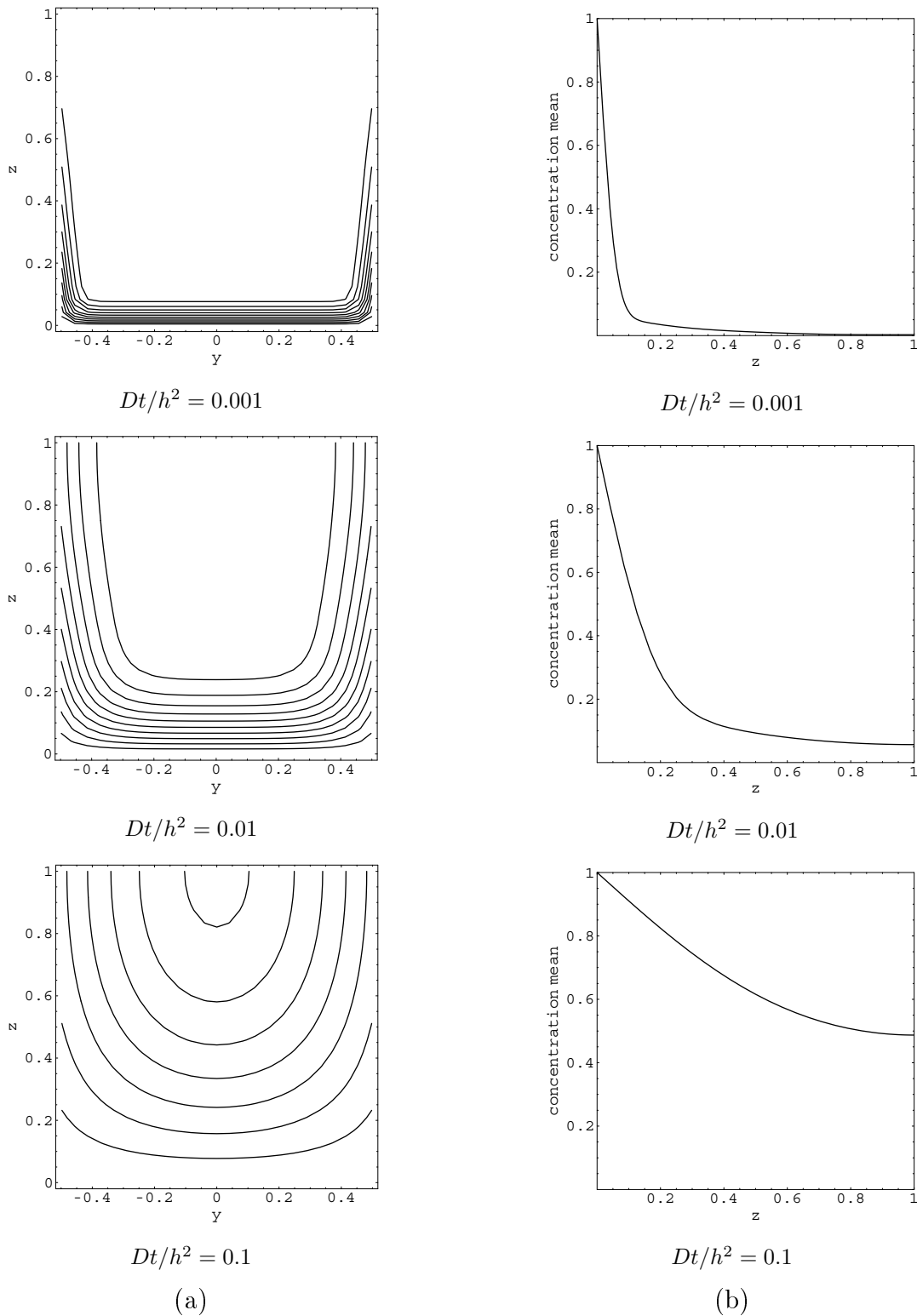


Figure A.6: (a) Iso-concentration contour plots (line spacing = $c_0/10$) in a grain of $d_s = h$ calculated for a thin film system of fixed $\Delta = D_b/D$ and different values of $t_f = Dt/h^2$ using Equation A.21. (b) The respective average-concentration profiles according to Equation A.24

A.3 XRD-Correction Factor

When evaluating results from a X-ray diffraction experiment and comparing the measured intensity to values derived from Equation (2.6) several additional effects have to be taken into account. The most important effects, which will be discussed below, arise from the following experimental “constraints” [168]:

- dispersion,
- polarization of incident and diffracted beam,
- sample rotation (Lorentz factor),
- temperature,
- geometry of sample and experimental set up,
- absorption,
- multiplicity.

Correction not applicable for polycrystalline powder samples, such as e.g. extinction, are not considered here.

Dispersion When deriving Equation (2.6) it is assumed that the x-ray wavelength is much smaller than any of the X-ray absorption edge wavelength of the atom in the crystal. Since this is not generally satisfied in an experimental situation, a dispersion correction for the atomic scattering factor has to be introduced:

$$f = f_0 + \Delta f' + i\Delta f'' , \quad (\text{A.27})$$

where f_0 is the tabulated value, and $\Delta f'$ and $\Delta f''$ are the real and imaginary parts of the dispersion correction. The correction is complex and accounts for a small shift in phase of the scattered radiation. The angular dependence of $\Delta f'$ and $\Delta f''$ is much smaller than that of f_0 [169]. The values used in this work are based on calculated values by Cromer and Libermann [92].

Polarization factor The polarization factor P accounts for the partial, angle dependent diffraction of incident radiation polarized parallel to the sample surface. For unpolarized incident radiation P is given by

$$P = (1 + \cos^2 2\theta)/2 . \quad (\text{A.28})$$

Lorentz factor During an experiment the crystal (or the incident beam) is usually rotated at a constant angular velocity ω about an axis parallel to the planes hkl and normal to the primary beam (crystal axis). The time Δt during which the incident beam makes roughly the right angle to satisfy the Bragg law, i.e. $|\mathbf{k}| \pm \Delta k = |\mathbf{G}|$ is different for

different lattice planes and can be expressed as ([168] p.85)

$$\Delta t = \frac{|\Delta k|}{|\omega|} L \quad \text{where,} \quad L = \frac{\lambda}{\sin 2\theta}. \quad (\text{A.29})$$

$|\Delta k|$ and ω are given for a certain experiment. The quantity L is called the Lorentz factor.

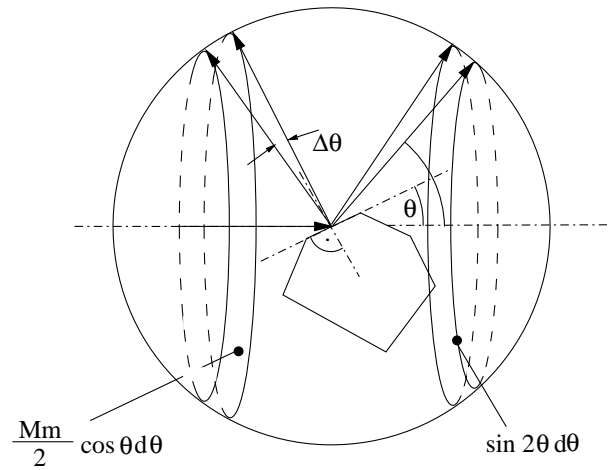
Temperature factor Equation 2.5 is based on the assumption that the atoms occupy a definite position in the crystal. However, even at room temperature the thermal oscillation and the resulting momental displacement may be appreciably. According to Warren, who has given a derivation that includes temperature vibration, equation 2.5 has to be replaced by

$$I(\mathbf{G}) = K \frac{I_0}{r^2} N^2 F_T^2(\mathbf{G}) |F_0(\mathbf{G})|^2, \quad \text{where,} \quad F_T^2(\mathbf{G}) = \sum_{\alpha} f_{\alpha} e^{-M_{\alpha}} e^{-i\mathbf{G}\cdot\mathbf{r}_{\alpha}}. \quad (\text{A.30})$$

where f_{α} is the atomic form factor, and $M_{\alpha} = B \sin^2 \theta / \lambda^2$ is a factor called Debye-Waller temperature factor.

Geometry factor The geometry of the experimental set up leads to a number of systematic errors which require additional corrections. When using polycrystalline or powder

Figure A.7: Geometry factor of a powder sample. The area $Mm/2 \cos \theta d\theta$ refers to the number of crystals in a powder sample whose hkl planes make angles between $\theta + d\theta$ with the primary beam. The area $\sin 2\theta d\theta$ refers to the cone of diffracted beams.



samples, as in this work, the sample contains an enormous number of very small crystals having (in the ideal case) completely random orientations. The number of crystals, with the right orientation to cause a Bragg reflection at 2θ , is proportional to $\cos \theta$ (Fig. A.7). The individual crystals can have any orientation around the incident beam. As a result the diffracted beams at a fixed angle 2θ with the incident beam form a cone of half apex angle 2θ . Since the total power belonging to the reflection is spread out over the elements of this cone, the recorded intensity is proportional to the power per unit length of the

diffraction circle, i. e. $1/\sin 2\theta$. If the receiving surface is at a constant distance from the sample the geometrical factor for a powder sample is

$$G(\theta) = \cos \theta / \sin 2\theta. \quad (\text{A.31})$$

Absorption factor When the incident X-ray beam penetrates into the sample its intensity is weakened due to the photo effect. The relative loss in intensity at a certain penetration depth Δx can, to a good approximation, be treated as isotrop and independent of intensity, so $\Delta I/I = -\mu\Delta x$, where μ is the linear X-ray absorption coefficient of the sample. For a Bragg-Bretano geometry (Figure A.8 (a)) the integral diffracted intensity is proportional to

$$I \propto I_0 \int_0^x e^{-2\mu x'} dx' = I_0 \frac{1}{2\mu} (1 - e^{-\mu \frac{2d}{\sin \theta}}). \quad (\text{A.32})$$

If $\mu d \gg 1$ the absorption correction simplifies to $1/2\mu$, i.e. is independent of the refractive angle 2θ . The linear X-ray absorption coefficient of a substance $(A_1)_{n_1}(A_2)_{n_2} \dots (A_q)_{n_q}$ depends on the mass density ρ and the linear mass absorption coefficient μ_m of the atoms composing the compound

$$\mu = \rho \frac{\sum_{i=1}^q n_i A_i (\mu_m)_i}{\sum_{i=1}^q n_i A_i}. \quad (\text{A.33})$$

Values for μ_m for a selection of the most common wavelength used in X-ray diffraction can be found e.g. in [169].

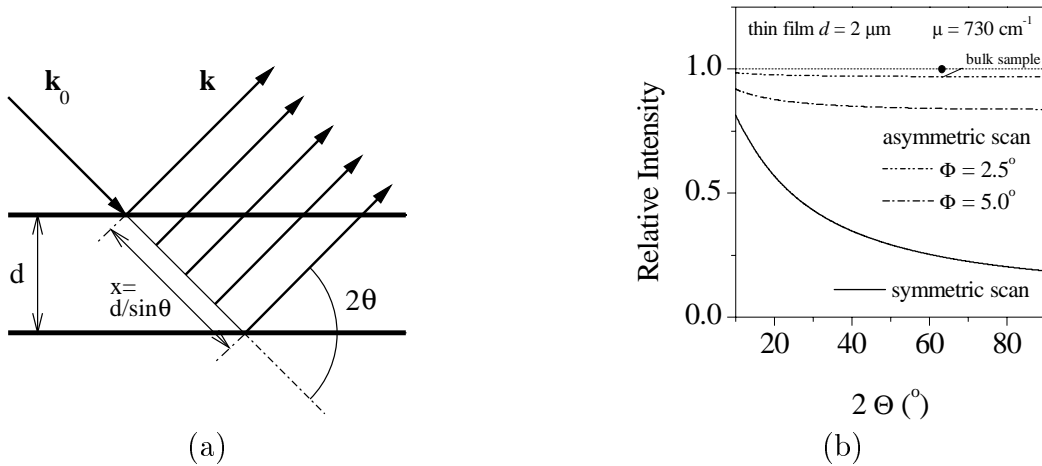


Figure A.8: (a) Experimental geometry for calculation of the absorption correction of a thin film sample when measuring in Bragg-Bretano geometry.

When investigating thin films $1/\mu$ is usually of the order of d or greater, hence the observed intensities especially at higher 2θ values is significantly reduced. This has to be considered when comparing thin film XRD-spectra to standard powder patterns from a reference data base. One way to increase the intensity is measuring in asymmetric Bragg mode, where the

incident angle is fixed at a small value ($\theta = 1.0^\circ - 5.0^\circ$) and only the detector is scanned (Figure 2.10). Figure A.8 (b) compares the 2θ dependence of the reflected intensity for a thin film powder sample of $\mu d = 0.15$ measured in symmetric and in asymmetric mode with respect to a bulk powder sample. Especially at higher 2θ values the gain in scattered intensity when measuring in asymmetric mode, can clearly be seen.

Multiplicity The multiplicity factor arises from the fact that in general there will be several sets of hkl -planes, having different orientation in the crystal, but which are equivalent in that they have the same d and $|F|^2$ values. In other words the multiplicity of a reflection is given by the number of variations in position and sign which can be given to $\pm h$, $\pm k$, $\pm l$ and have the same $|F_{hkl}|^2$. For a tetragonal unit cell the maximum multiplicity is 16.

A.4 XRD Simulation Parameters

The parameters used for calculating XRD-spectra are listed in the following.

Dispersion $f = f_0 + \Delta f' + i\Delta f''$

Reference: Cromer and Libermann [92].

atom	$\Delta f'$	$\Delta f''$
Cu	-2.019	0.589
In	-0.126	5.045
Ga	-1.345	0.777
S	0.319	0.577

Debye-Waller temperature factors See Equation (A.30)

Reference: Abrahams and Bernstein [23].

atom in CuInS ₂	B (Å)
Cu	1.42 ± 2
In	0.76 ± 2
S	0.83 ± 2

atom in CuGaS ₂	B (Å)
Cu	1.60 ± 2
In	1.02 ± 2
S	1.02 ± 2

Linear mass absorption coefficients μ_m See Equation (A.33)

Reference: Haussühl [168]

atom	μ_m ($10^2 \text{ mm}^2/\text{g}$)
Cu	52.9
In	243.0
Ga	67.9
S	89.1

A.5 Phases Diagrams

Copper-Sulfur

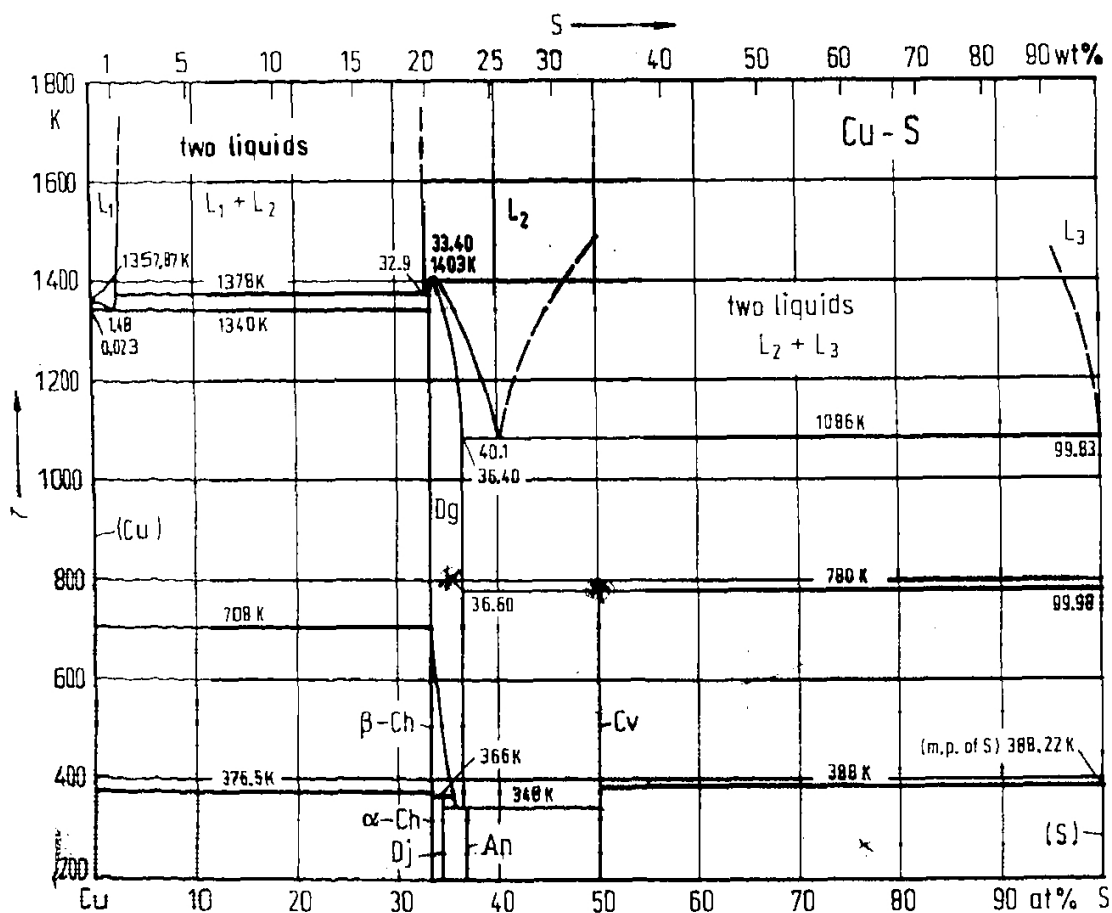


Figure A.9: Cu-S phase diagram (from Ref. [99]).

Copper-Gallium-Sulfur

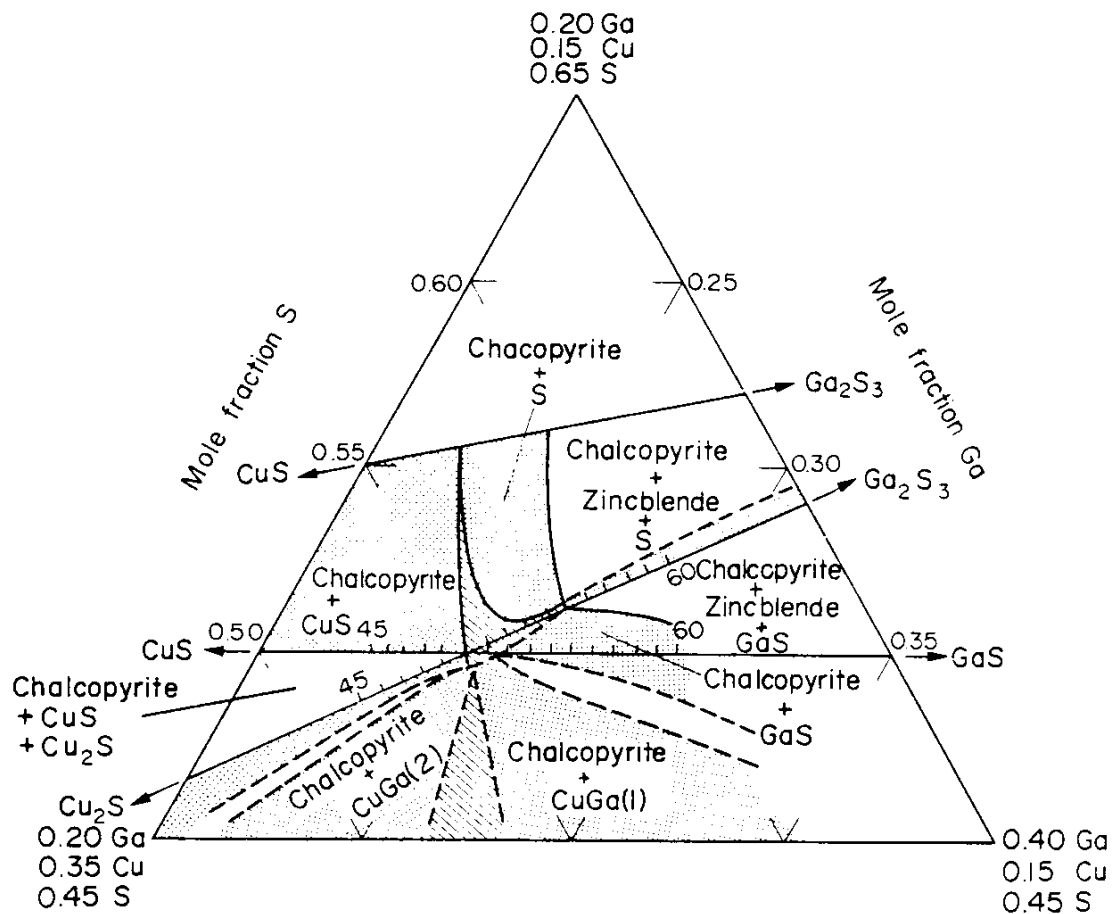


Figure A.10: Ternary phase fields around CuGaS_2 . Chalcopyrite phase region is denoted by cross-hatched area (from Ref. [170]).

